Research Report

Thrust Force Analysis of Tripod Constant Velocity Joint Using Multibody Model

Hideki Sugiura, Tsugiharu Matsunaga, Yoshiteru Mizutani, Yosei Ando and Isashi Kashiwagi

Report received on Mar. 21, 2011

■**ABSTRACT**‖ A tripod constant velocity joint is used in the driveshaft of front wheel drive vehicles. Thrust force generated by this joint causes lateral vibration in these vehicles. To analyze the thrust force, a detailed model is constructed based on a multibody dynamics approach. This model contains all principal parts of the joint defined as rigid bodies and all force elements of contact and friction acting among these parts. This model includes a new contact modeling method of needle roller bearings for more precise and faster computation. In this needle roller model, a cylindrical configuration is approximated by multiple spherical configurations. The appropriateness of this joint model is validated by comparing computational and experimental results. Moreover the factors inducing the thrust force are clarified by evaluating the contribution of friction forces at each contact region to the thrust force. That is, the principal factor of the third rotating order component of the thrust force is sliding friction between the roller and the groove, and the factor of the second rotating order component is sliding friction of skewed needle rollers.

1. Introduction

A tripod constant velocity joint is mainly used as an axle driveshaft inboard joint in front wheel drive vehicles. In a case where the driveshaft has an axial displacement in addition to a joint angle, this joint must transmit the driving torque generated by the engine. This joint therefore has a plunging mechanism permitting the axial displacement. However, this useful function also generates a housing axial thrust force whose amplitude periodically changes with the revolution of the driveshaft. In order to reduce this dynamic force, which induces lateral vibration in the vehicle, it is necessary to develop a computational method for this force and to clarify the factors causing it.

With respect to these problems, an equilibrium analysis method has already been proposed. In this method, the thrust force is obtained using equations of equilibriums on forces and moments.[1] However, in order to design the joint precisely, it is necessary to estimate the influence of the contact configuration and the dynamic behavior with respect to each part. On the other hand, a hypothesis for the principal factors inducing the thrust force has also been proposed. In this hypothesis, the thrust force is based on two sources. One is sliding friction and rolling friction between the spherical roller and the housing groove. Another is sliding friction between the spherical roller and the spider trunnion.[2-4] However, a reason for this hypothesis, based on computational or experimental results, has not been demonstrated.

This paper describes an analysis method of a tripod constant velocity joint based on a multibody dynamics approach. To analyze the thrust force, a detailed model is constructed. This model contains all principal parts of the joint as rigid bodies and all force elements of contact and friction acting among these parts. Here, general analysis models of needle roller bearings are simplified, but this joint model includes a new contact modeling method for the needle roller bearings for more precise and faster computation. The influence of skewed needle rollers on the thrust force is therefore clarified. Moreover, the appropriateness of this joint model is validated by comparing the computational and experimental thrust forces. This paper also describes the contribution of friction forces at each contact region to the thrust force and the principal factors inducing the thrust force.

2. Analysis model

2. 1 Mechanism of tripod joint

Figure 1 shows the tripod constant velocity joint. The housing acts as the input axis and includes three equally spaced grooves. The direction of these grooves is parallel to the input shaft. Each groove is configured as a half circular cylinder. The intermediate shaft acts as the output axis. The spider, which consists of three equally spaced trunnions, is connected to this shaft. The spherical roller is supported on the trunnion through multiple needle rollers. The driving torque is transmitted between the grooves of the input side and the spherical rollers of the output side.

2. 2 Outline of computational method

Figure 2 shows a schematic of the analysis model. The principal parts of the joint are defined as rigid bodies, which include both mass and inertia, and are located in a three-dimensional global coordinate system. A force element, which consists of contact force and friction force, connects each part, i.e., the groove in the housing, the spherical roller, the needle roller, and the trunnion on the spider. The clearance among these parts is considered based on the locations and contact configurations of the actual parts. Moreover, the input axis and the output axis are constrained with a reasonable joint angle.

The equations of motion in the multibody system are derived from this model. The equations can be described as follows.[5]

$$\begin{bmatrix} \mathbf{M} & \mathbf{\Phi_q}^T \\ \mathbf{\Phi_q} & 0 \end{bmatrix} \begin{bmatrix} \ddot{\mathbf{q}} \\ \lambda \end{bmatrix} = \begin{bmatrix} \mathbf{Q} \\ \gamma \end{bmatrix} \quad \cdots\cdots\cdots\cdots (1)$$
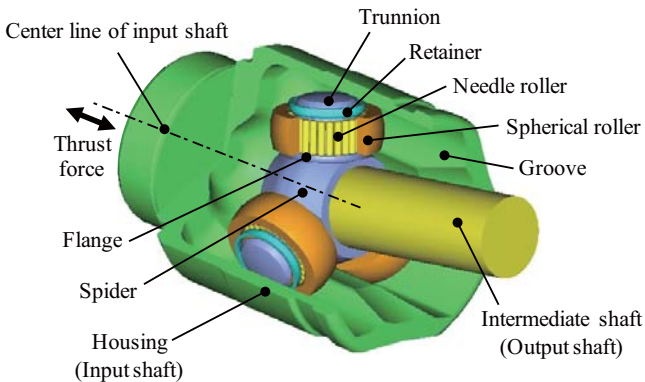
where $\mathbf{M}$ is the generalized mass matrix, $\ddot{\mathbf{q}}$ is the acceleration vector in the generalized coordinate system $\mathbf{q}$, $\mathbf{\Phi_q}$ is Jacobian and obtained by partial differentiation of the constraint equation $\mathbf{\Phi} \equiv \mathbf{\Phi}(\mathbf{q}, t) = 0$ based on $\mathbf{q}$ and time t, and $\mathbf{Q}$ is the generalized force vector, which consists of external forces (considering contact and friction force) and the terms of inertia using the square of angular velocity. γ is obtained by second order differentiation of $\mathbf{\Phi}$ as $\gamma \equiv \mathbf{\Phi_q}\ddot{\mathbf{q}} = -(\mathbf{\Phi_q}\dot{\mathbf{q}})_q\dot{\mathbf{q}} - 2\mathbf{\Phi}_{qt}\dot{\mathbf{q}} - \mathbf{\Phi}_{tt}$,

$\mathbf{\Phi}_{qt} = \left[\partial^2\Phi_i / \partial q_j\partial t\right]_{nh\times nc}$, and $\mathbf{\Phi}_{tt} = \left[\partial^2\Phi_i / \partial t^2\right]_{nh\times 1}$, where nh is the number of the holonomic constraint and nc is the number of the generalized coordinate system. These differential-algebraic equations of motion are solved and the thrust force is derived from the axial reaction force in the housing.

In the actual analysis, the commercial software DADS[6] is utilized for developing the analysis model and solving the equations of motion numerically.

2. 3 Contact and friction model

Figure 3 shows a schematic diagram of the contact and friction model. When each contact surface attached on two rigid bodies overlaps, the contact force derived from the penetration of this overlap acts on each point of contact of the two rigid bodies. If a relative velocity between the two rigid bodies exists at the point of contact, the friction force works toward the tangential direction. If a relative angular velocity between the two rigid bodies exists, spinning moment acts around the normal vector of the point of contact. Moreover, if relative rolling between the two bodies appears, rolling resistant moment is generated. These equations are described as follows.
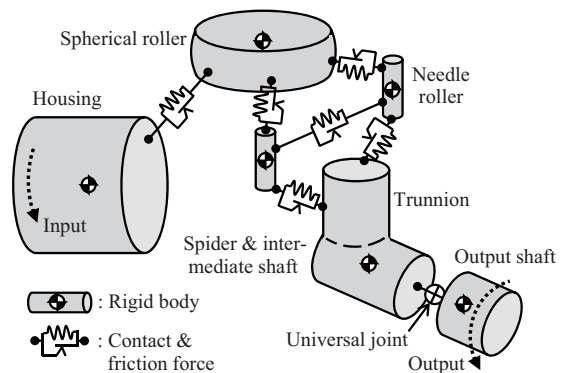

Fig. 1   Tripod constant velocity joint.

Fig. 2   Schematic of multibody model of tripod joint.

The contact force f_n is the power of the penetration δ [mm] and defined by

$$f_n = C\,\delta^m \quad \cdots\cdots\cdots\cdots\cdots\cdots\cdots (2)$$

where m is the exponent of the power and C is the coefficient. These values are set up according to contact configuration.

The friction force f_t is derived from a multiplication of the contact force and the sliding friction coefficient μ_s and defined by

$$f_t = \mu_s f_n \quad \cdots\cdots\cdots\cdots\cdots\cdots\cdots (3)$$

where μ_s is the dynamic friction coefficient. Here, μ_s contains the hyperbolic tangent function shown in **Fig. 4** in order to model the friction force, which increases continuously from zero relative velocity.

The rolling resistant moment M_r can be discussed as follows. In a case where the resistant force F is generated by rolling a needle roller between two plates under the load P, as shown in **Fig. 5**, the rolling friction coefficient is defined as $\mu_r = F/P$.[7] Here, the rolling resistant moment is derived from a multiplication of F and D. Considering that this moment contains

resistance concerning two points of contact, it is actually represented as follows.

$$M_r = F D / 2 = \mu_r P D / 2 \quad \cdots\cdots\cdots\cdots\cdots (4)$$

μ_r also includes the hyperbolic tangent function.

The configuration of each contact region is explained in the following sections. It is also described how the exponent m and the coefficient C are obtained.

2. 3. 1 Contact between spherical roller and groove

The contact surface of the roller is a sphere, and the contact surface of the groove is a half circular cylinder. Using Hertz's theory of elasticity, in the case of steel, the elastic penetration δ_{ro} [mm] is defined as follows [8]:

$$\delta_{ro} = 2.79 \times 10^{-4}\,\frac{2K}{\pi\mu}\sqrt[3]{\Sigma\rho \cdot f_n^2} \quad \cdots\cdots (5)$$

where ρ [1/mm] is the curvature of the contact surface and $2K/\pi\mu$ is the coefficient determined by the curvature. By converting this equation using Eq. (2) or the like, m and C are obtained as shown in **Table 1**.

This section also discusses the spinning moment M_s. The contact ellipse between the sphere and the cylinder has a ratio of 20 to 1. In the case where the major axis
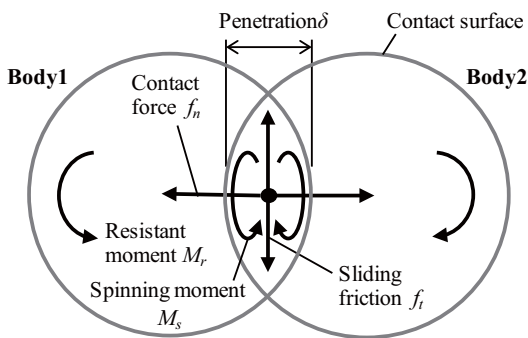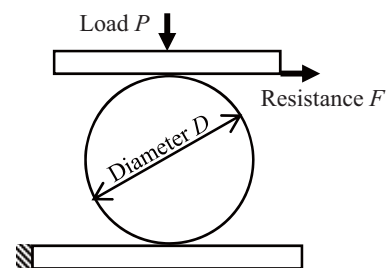

Fig. 3   Schematic of contact model.

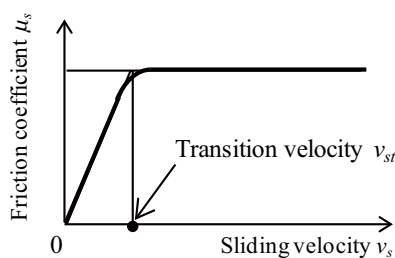**Fig. 4**   Function on sliding friction coefficient.

Fig. 5   Definition of rolling friction.

Table 1   Details of exponent m and coefficient C.

Object	Spherical roller vs. groove	Needle roller vs. other parts
m	$3/2$	$10/9$
C	$\dfrac{2.15\times10^5}{\sqrt{(2K/\pi\mu)^3\,\Sigma\rho}}$	$8.15\times10^4\,\dfrac{l^{8/9}}{N_s}$

radius of the contact ellipse is $2a$ [mm], the spinning moment is approximated as follows.[9]

$$M_s = (3/8)\,\mu_s f_n\, a \cdots\cdots\cdots\cdots\cdots\cdots (6)$$

In the case of steel, by using the coefficient μ based on the curvature of the contact surface by Hertz's theory, a is defined by $2a = 0.0472\mu \sqrt[3]{f_n/\Sigma\rho}$ [8]. M_s is therefore defined by

$$M_s = 8.85\times10^{-3}\,\frac{\mu}{\sqrt[3]{\Sigma\rho}}\,\mu_s f_n^{4/3} \quad\cdots\cdots\cdots (7)$$

2. 3. 2 Contact between needle roller and other parts

The needle roller configured as a cylinder touches the trunnion, the inside surface of the spherical roller, and the other needle rollers located on both sides, respectively. These parts are also configured as cylinders. On the other hand, the analysis model of the joint takes the clearance among all parts into account, and the needle roller has 6 degrees of freedom. Several contact conditions therefore occur, as shown in **Fig. 6**: equal line contact in the case of two parallel axes, unequal line contact in the case of two inclined axes, and point contact in the case of two skewed axes. These conditions mutually change at all times. Moreover, if relative sliding velocity and/or relative angular velocity exists, sliding friction and/or spinning moment is added.

In order to efficiently simulate the multiple contact phenomena mentioned above, a new modeling method is proposed that discretely approximates line contact using multiple point contacts. The number N_s of spherical configurations with the same diameter 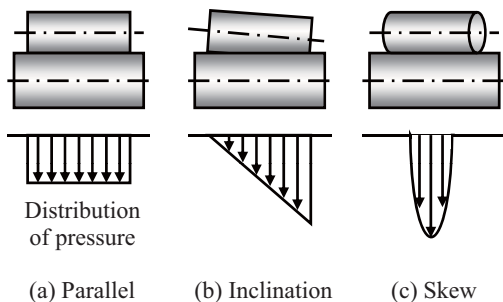as the needle roller are prepared, and a contact surface is constructed that arranges these spheres in a line. The needle roller model has this contact surface and is defined as a rigid body with the inertia of a cylinder. The contact forces in this contact surface therefore act as the arrows in Fig. 6, which show the distribution of contact pressure. Here, the edge load in which the contact force increases at the end of a line contact is disregarded.

Figure 7 shows a schematic of this contact model. Each spherical configuration touches three kinds of cylindrical contact surfaces: the trunnion, the inside of the spherical roller, and the next needle roller. The flange of the trunnion and the retainer on the trunnion are also modeled using the contact elements to prevent the needle rollers from springing out. The total number of this needle roller model needs to be the same as the number N_n of the needle rollers, which is used on the trunnion, in order to construct the bearing.

Next, the contact force of each sphere is formulized. It is clarified that the elastic penetration δ_{ne} [mm] between two parallel cylinders is independent of the curvature of each cylinder and is dependent on the load and the length of the line contact.[10] Therefore, in the case of steel, this is,

$$\delta_{ne} = 3.8\times10^{-5}\,(N_s f_n)^{0.9}/l^{0.8} \cdots\cdots\cdots\cdots (8)$$

where f_n is the contact force on one sphere and l [mm] is the length of the contact region. The exponent m and the coefficient C, as shown in Table 1, can be obtained by converting this equation using Eq. (2) or the like.

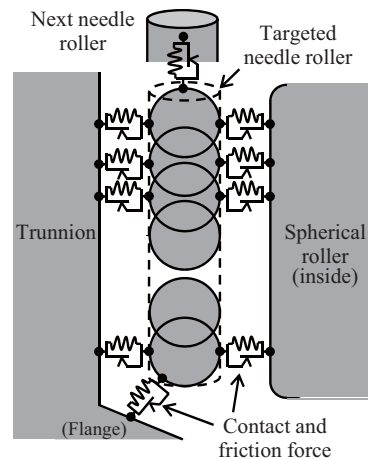This section also explains the spinning moment. Friction force works at each contact point on spheres.

Distribution of pressure

(a) Parallel   (b) Inclination   (c) Skew

Fig. 6 Contact modes of needle roller.

Next needle roller   Targeted needle roller

Trunnion   Spherical roller (inside)

(Flange)   Contact and friction force

Fig. 7 Contact model set of needle roller.

If the needle roller is rotating toward the skew direction, the spinning moment is considered based on the summation of moments corresponding to the distance from the skew center to each contact point.

2. 3. 3 Validation of needle roller model

A skewed needle roller, which rolls between two plates, draws a characteristic locus influenced by the axial friction force.[10] The needle roller model is validated using this example.

A needle roller is located between the fully constrained plate A and the loaded plate B as shown in **Fig. 8**(a). Plate B is constrained with the constant velocity (and is also constrained on the other degrees of freedom). It is supposed that φ is the skew angle and μ_{sA} and μ_{sB} are the sliding friction coefficients between the needle roller and each plate, respectively. The locus of the needle roller center is obtained as shown in Fig. 8(b): the solid line in the case of $\mu_{sA} = \mu_{sB}$, the broken line in the case of $\mu_{sA} > \mu_{sB}$, and the chain line in the case of $\mu_{sA} < \mu_{sB}$. Since the characteristic of these loci is the same as the result shown in ref.(10), the validity of the needle roller model is clarified.

2. 4 Constraint conditions

The housing, which acts as the input axis, is given a rotational driving constraint, and the other degrees of freedom are also constrained. The intermediate shaft is connected to an output shaft defined as a rigid body, using a so-called universal joint (simulating an outboard joint simply as shown in Fig. 2). This output shaft is constrained in order to keep the proper joint angle between the input axis and the intermediate

shaft, except in the rotational direction around the output axis where torque is loaded. Finally, the spherical roller and the needle roller have 6 degrees of freedom respectively. The intermediate shaft has 2 degrees of freedom, and the output shaft has 1 degree of freedom. The total degrees of freedom are obtained by

$$6 \times 3\,(1 + N_n) + 2 + 1 = 18N_n + 21 \cdots\cdots\cdots (9)$$

3. Analysis results and study

3. 1 Analysis conditions

The joint is analyzed under a rotational speed of 600 rpm, a torque of 50 Nm, and a joint angle of 10 degrees. The location and configuration of each part of the actual joint, which has twenty-seven needle rollers, are utilized in the analysis model. The number of spheres of one needle roller model is seven. As shown in **Fig. 9**, a skewing case where the needle roller inclines counterclockwise to the normal direction on the surface of the trunnion is defined as positive.

With respect to the friction coefficients, the sliding friction coefficient between the spherical roller and the groove is 0.05, the sliding friction coefficient between the needle roller and other parts is 0.03, and the rolling friction coefficient is 0.002. These values are measured using greased test pieces. So that the friction force acts with a low relative velocity, the transition velocity v_{st}, that is, the criterion to change to a constant friction (shown in Fig. 4), is defined as one fourth of the maximum sliding velocity in the analysis results. The same rule is applied in the case of the rolling friction.
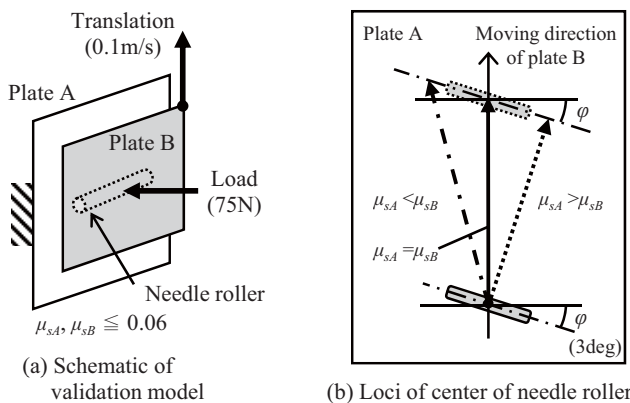

(a) Schematic of validation model

(b) Loci of center of needle roller

Fig. 8   Validation of contact model of needle roller.
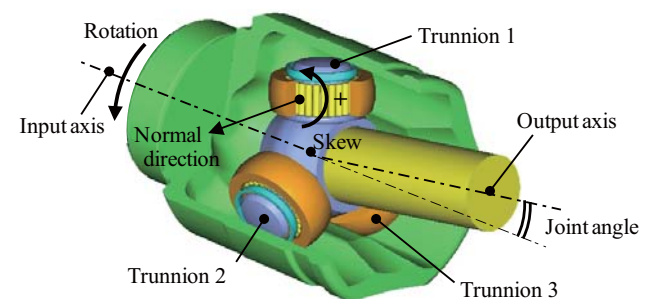

Fig. 9   Definition concerning trunnions and skew direction.

3. 2 Analysis results of thrust force

Figure 10 shows two waveforms of the thrust force with respect to different initial skew angles. Here, the horizontal axis shows the rotational phase angle of the joint. The third and fourth cycles from the beginning of the analysis are used in these waveforms. The origin of the rotational phase angle is the position where the center of the spherical roller is located between the input axis and the output axis in the plane composed by these two axes (shown by trunnion 1 in Fig. 9). The angles illustrated in Fig. 10 are initial skew angles and are applied to all needle rollers on trunnions 1, 2, and 3 in turn. With respect to the waveforms shown in Fig. 10, the third rotating order component is clearly evident. Moreover, a beat occurs in the waveform of analysis case 2 as shown by the envelope in Fig.10. This is concerned with the initial skew angles.

Figure 11 shows the skew angles, comparing the value in the fourth cycle with the initial value. The initial value, maximum value, and minimum value in one cycle are shown simultaneously. These values are derived from the needle roller, which strongly contacts each trunnion. Since extreme changes are not observed
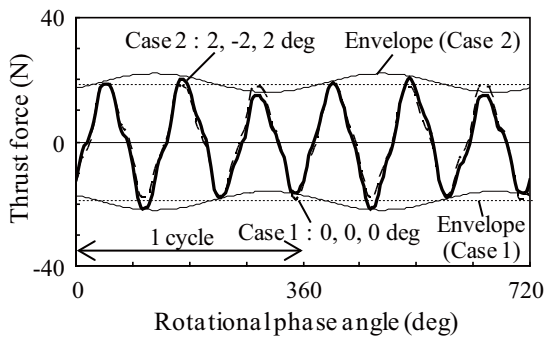
in these skew angles, it is possible to represent the magnitude of the skew angle by the initial value.

3. 3 Comparison with experimental results

Thrust force is measured using a commercial apparatus under the same conditions as the analysis. **Figure 12** shows the measured waveform. The third rotating order component appears in the same way as in the analysis result. In this case, the beat also occurs as in analysis case 2, but the phase of the beat is different. The reason for this is described later. By the way, it is inferred that the factor inducing the beat is the second or the fourth rotating order component because this beat has a first rotating order component. Here, as shown in **Fig. 13**, rotational order tracking analysis on the experimental thrust force shows that the second rotating order component is more evident than the fourth. Thus, it is confirmed that the factor inducing the beat is the second rotating order component.

This section discusses the influence of the joint angle. **Figure 14** shows the effective values of the second and third rotating order components for the
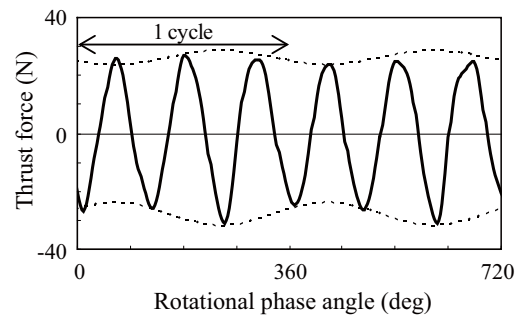

Fig. 10 Computational results of thrust force.

Fig. 12 Experimental result of thrust force.

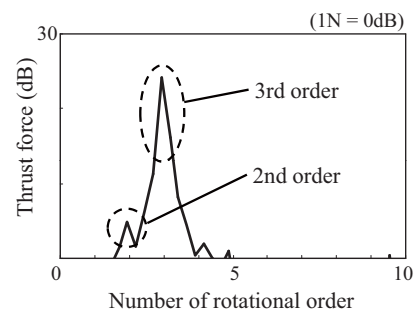**Fig. 11** Investigation of computational skew angle.

Fig. 13 Result of rotational order tracking analysis.

computational and experimental results. The third rotating order component is the principal factor inducing the thrust force. In this case, virtually no difference between computational case 1 and 2 is observed. Moreover, the proportional relationship of the computational results to the joint angle is the same as in the experiment. The second rotating order component is the factor inducing the beat. In this case, the difference between computational case 1 and 2 corresponds to the magnitude of the initial skew angle, and both cases are independent of the joint angle. On the other hand, the experimental results fluctuate at random.

In addition, it is clarified that the third rotating order component has a proportional relationship to the driving torque and is independent of the rotational speed, by analyzing the experimental results. In the case of the computational results, the same tendency is found.

3. 4 Consideration on thrust force

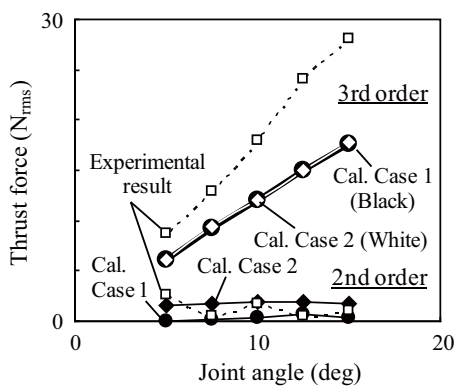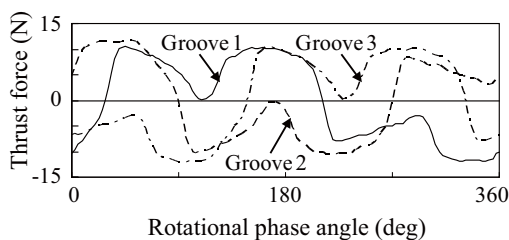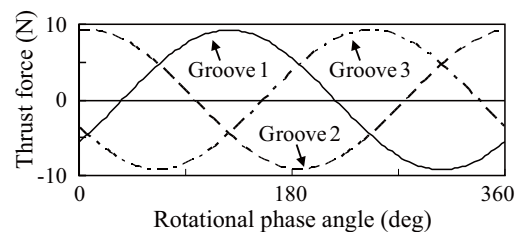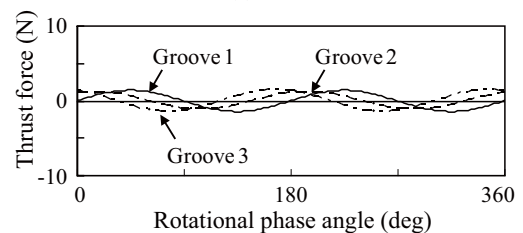This section discusses the local thrust force induced at an individual groove in order to clarify the factors inducing the thrust force. Taking analysis case 2 where the beat occurs as an example, **Fig. 15** shows the waveforms of the local thrust forces at three grooves. Grooves 1, 2, and 3 correspond to the turns of the trunnions 1, 2, and 3. Next, **Fig. 16** shows the waveforms for the three components, since the result of the rotational order tracking analysis for the local thrust force indicates that the first, second, and third rotating order components are dominant.

Although the first rotating order component is contained in the local thrust forces, it is nearly zero in the summed thrust force. This is because each phase angle of this component is different by 120 degrees according to the equally arranged grooves. On the other hand, in the case of the third rotating order component, the interval of each phase angle is the same as one cycle. Therefore, the summed third order rotating component is three times of the amplitude of the local component.
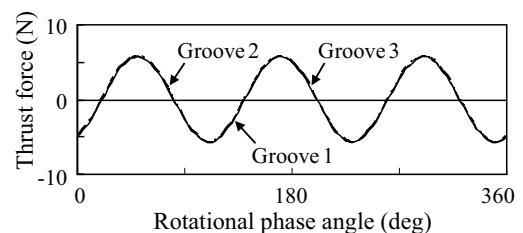
The summed second rotating order component is amplified by the overlap of the local components and becomes the factor generating the beat. This overlap occurs as a result of the irregular phase angles of these local components, although the grooves are equally

Fig. 14 Variation of thrust force with joint angle.

Fig. 15 Computational result of local thrust force at each groove.

Fig. 16 Waveforms of dominant component of thrust force at each groove.

arranged. Here, the reason of this irregular phase angle is concerned with the influence of the skew directions of the needle rollers. **Figure 17** based on Fig.16(b) shows the waveforms illustrated with the individual skew angles. It is possible to understand that the skew angle of the local component of the groove 2 is opposite to the others. Next, as shown in this figure, when the skew direction at the groove 2 is reversed, the interval of each phase angle becomes regular. In this case, the beat does not occur because all the components cancel each other out. In the same way, when all skew directions of analysis case 2 are reversed, the phase angle of the beat changes. In order to confirm these, new analysis cases 3 and 4 are calculated. In case 3, the initial skew angles are the same directions. In case 4, all initial skew angles based on case 2 are reversed. **Figure 18** shows the wave forms of the thrust force in these cases. The result of case 3 shows no beat. The phase angle of the beat in case 4 is different from that in case 2, and the difference between these phase angles is 180 degrees. Finally, it is clarified that the beat in the waveform of the thrust force is an irregular phenomenon depended on uneven skew of the needle rollers. Here, the following cases are excluded: where the skew angles of all trunnions are nearly zero, and where both the

skew angles and the skew directions on all trunnions are nearly equal. Thus, the following facts can be explained: (1) the phase angle of the beat of the computational result is different from the experimental one as described in § 3.3, and (2) the experimental effective value of the second rotating order component shown in Fig.14 fluctuates irregularly according to the variation of the joint angle (because the initial conditions of the needle rollers changes simultaneously).

3. 5 Contribution of friction forces on thrust force

It is necessary to grasp contributions of the contact region and the friction force on the second and third rotating order components of the thrust force. A parameter study is performed for the contact region and the friction force in order to estimate the contribution for case 2. **Figure 19** shows this contribution.

The principal factor inducing the third rotating order component is sliding friction between the spherical roller and the groove. The contribution of other types of friction is as follows: the spinning moment and the rolling friction between the spherical roller and the groove are 2% and 5%, respectively, and the rolling friction of the needle rollers is 6%. As an example to explain this principal factor, **Fig. 20** shows the computational results based on case 2, concerning the sliding friction between the spherical roller and the groove. The amplitude of the waveform fluctuates according to the sliding friction. Here, it is supposed that this friction force is caused by disagreement between the rolling and traveling directions of the spherical roller.

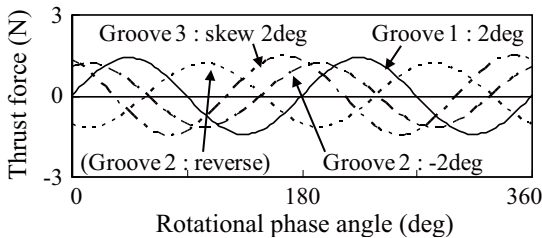On the other hand, since the sliding friction of the
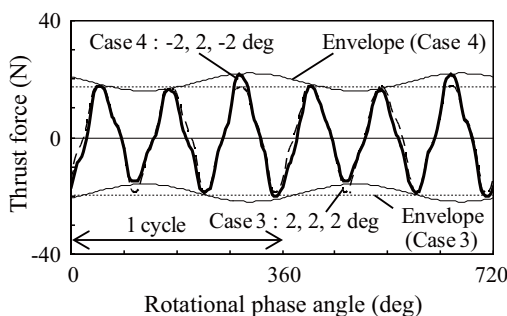

Fig. 17　Enlargement of 2nd order.

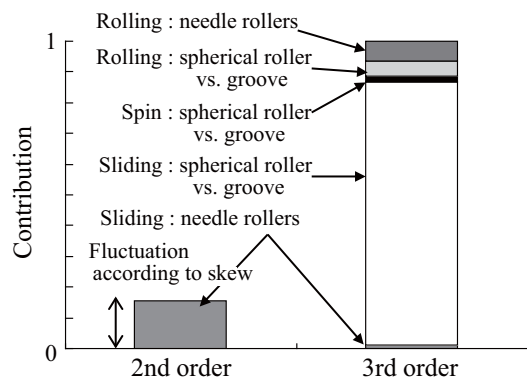**Fig. 18**　Computational result of thrust forces concerning different skew angles.

Fig. 19　Contribution of friction on components.

needle rollers is mainly concerned with the second rotating order component, the contribution to the third rotating order component is 1%. This friction is induced in a case where the skewed needle roller is rolling.

4. Conclusions

This research constructs an analysis model of a tripod constant velocity joint based on multibody dynamics in order to analyze the thrust force caused in the joint. The appropriateness of this model is validated by comparing computational and experimental results. This research also shows the influence of skewed needle rollers on the thrust force, evaluates the contribution of friction forces at each contact region to the thrust force, and obtains useful knowledge about the principal factors inducing the thrust force. These results are summarized as follows:

(1) The analysis model includes all principal parts as rigid bodies and all elements of contact force and friction force acting on these parts. In particular, the needle roller model is approximated by multiple spherical configurations. The computational results with this model agree well with the experimental results in the following characteristics; (a) In the waveform of the thrust force, the third rotating order component is clearly evident and the beat caused by the second rotating order component is also observed. (b) The effective value of the third rotating order component is in proportion to the joint angle.

(2) The principal factor of the third rotating order component is sliding friction between the spherical roller and the groove. This component occurs at individual grooves and the amplitude of this

component becomes three times larger because there are three grooves.

(3) The factor of the second rotating order component is sliding friction of needle rollers. Since the amplitude and/or the phase of this component fluctuates in accordance with the angle and/or the direction of the skewed needle rollers, a beat occurs irregularly.

References

(1) Watanabe, K., Kawakatsu, T., Nakao, S. and Ohara, T., "Analyses of Static Characteristics of Tripod Constant Velocity Joints", *Transactions of the Japan Society of Mechanical Engineers*, *Series C* (in Japanese), Vol.66, No.650 (2000), pp.3441-3448.

(2) Dodge, J. H. and Wagner, E. R., *Universal Joint and Driveshaft Design Manual* (1979), p.131, SAE.

(3) Kimata, K., "Friction and Lubrication of Constant Velocity Joints", *Journal of Japanese Society of Tribologists* (in Japanese), Vol.31, No.10 (1986), pp.697-702.

(4) Shimizu, M., Kobayashi, M. and Okamura, M., "Amelioration of Vibration and Noise by Reducing Vibromotive Force on the Constant Velocity Joints", *Mitsubishi Motors Technical Review* (in Japanese), No.3 (1990), pp.37-45.

(5) Haug, E. J., *Computer-Aided Kinematics and Dynamics of Mechanical Systems : Basic Methods,* Vol.1 (1989), pp.218-229, Allyn & Bacon.

(6) Computer Aided Design Software, Inc. ed., *DADS Revision8.0 Reference Manual* (1997), Computer Aided Design Software, Inc.

(7) Okamoto, J., Nakayama, K. and Sato, M., *Toraiboroji Nyuumon* (in Japanese), (1990), p.115, *Saiwai Syobo*.

(8) Brändlein, J., Eschmann, P., Hasbargen, L. and Weigand, K., *Ball and Roller Bearings : Third Edition* (1995), Wiley.

(9) Harris, T. A., *Rolling Bearing Analysis* (1966), p.437, Wiley.

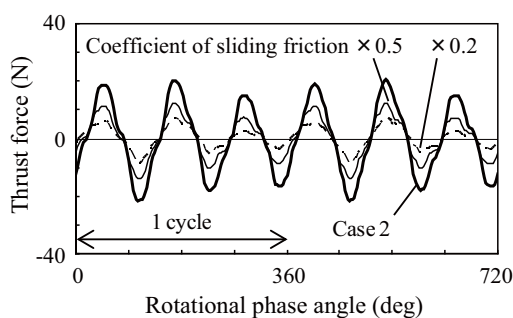(10) Okamoto, J. and Nozawa, Y., *Shinjokorojikuuke* (in Japanese), (1991), p.111, *Koyo Seiko*.

Fig. 20 Computational results concerning sliding friction between spherical roller and groove.

Hideki Sugiura
 Research Fields :
  - Application of multibody dynamics
  - Development of suspension design
   method
 Academic Society :
  - The Japan Society of Mechanical Engineers
  - Society of Automotive Engineers of Japan
 Awards :
  - The Japan Society of Mechanical Engineers
   Design & Systems Conference 2008 Best Poster
   Award, 2008
  - The Japan Society of Mechanical Engineers
   Dynamics & Design Conference 2009 Best
   Presentation Award, 2010

Tsugiharu Matsunaga
 Research Field :
  - Automotive hydraulic system
 Academic Societies :
  - The Japan Society of Mechanical
   Engineers
  - Society of Automotive Engineers of Japan

Yoshiteru Mizutani
 Research Fields :
  - Development of the load measurement
   transducer
  - Test and research on the structural
   strength of the vehicle

Yosei Ando*
 Research Field :
  - Development of constant velocity joints

Isashi Kashiwagi*
 Research Field :
  - Development of constant velocity joints
 Academic Society :
  - Society of Automotive Engineers of
   Japan

* JTEKT Corporation